COMMUNICATION

Unidirectional, Highly Linear Strain Sensors with Thickness-Engineered Conductive Films for Precision Control of Soft Machines

Received 00th January 20xx,
Accepted 00th January 20xx

DOI: 10.1039/x0xx00000x

Saeb Mousavi [a,d], Mai Thanh Thai [b], Morteza Amjadi [c], David Howard [d], Shuhua Peng [a], Thanh Nho Do [b], Chun H. Wang*[a]

Current stretchable strain sensors possess limited linear working ranges and it is still a formidable challenge to develop sensors that concurrently possess high gauge factors and high stretchability (ε ~ 100%). Herein, we report a facile method for creating unidirectional strain sensors to address the above issues. Using the 3D printing technique, we introduced thickness variations to control microcracking patterns in a carbon nanofibers-containing PEDOT:PSS (poly(3,4-ethylene dioxythiophene) polystyrene sulfonate) thin-film sensor. As a result, the sensor is capable of exceptionally linear response for up to 97% tensile strain while maintaining a high gauge factor of 151.

1 Introduction

There is a growing interest in soft sensor technologies that can couple high compliance and safety with high sensitivity for a wide range of applications including soft robotics [1-3], healthcare [4, 5], surgery [6-9], and wearable systems [10-14]. Over the past few years, many studies have focused on the creation of stretchable strain sensors with high stretchability [15-21] or high sensitivity [22-32]. Although some existing soft strain sensors could simultaneously achieve good sensitivity and high stretchability [33-36], their linear response to mechanical deformation remains limited. Furthermore, the majority of stretchable sensors exhibit high levels of nonlinearity, thus limiting their use in practice. For sensors with a nonlinear relationship between their output and the applied strain, complicated signal processing is required to accurately measure the applied mechanical strain. In addition, many stretchable strain sensors are approximately omnidirectional (have a similar sensitivity in all directions), making it difficult to map strain distributions in complex 2D or 3D objects. Therefore, there is a considerable need to develop unidirectional or strongly directional stretchable strain sensors offering high linearity and sensitivity over a wide working range.

An effective strategy for achieving high sensitivity is to generate microcracks in thin-film strain sensors where the opening and closing of microcracks under dynamic loading result in significant changes in the electrical resistance and subsequent enhancement of sensitivity. Lee et al. [36] proposed a fibre-based strain sensor with a working strain range of up to 200%, composed of cracked Ag-rich shells with a multi-filament structure. However, the sensor exhibited highly non-linear behaviour. In thin-film strain sensors, the length and opening width of the microcracks are proportional to the film thickness [37], and the sensitivity of sensors enhances with the average microcrack length [38]. Although the sensitivity can be greatly improved by increasing the thickness of the thin films, the formation of channel cracks (*i.e.*, large cracks across the entire width of the sensors) significantly reduces the stretchability of strain sensors.

To address the issue of channelling of microcracks in thin-film sensors, researchers have proposed mitigating techniques to increase the stretchability by using hybrid materials (nano-bridging) or by using structural engineering (variable or gradient thickness and by introducing wrinkles). Peng et al. [33] reported a nano-toughening mechanism to significantly increase the linear operation range of microcrack-based PEDOT:PSS sensors, achieving a linear strain range of 201% with a moderate sensitivity or gauge factor (GF) of 23. These sensors typically have a uniform thickness and feature a low sensitivity. Zhou et al. [45] fabricated a tunable and nacre-mimetic multifunctional e-skin for ultra-sensitive contact (strain sensing) and noncontact (humidity sensing) sensing based on multilayered AgNWs/rGO/TPU mats. The sensors possessed a tunable

[a] School of Mechanical and Manufacturing Engineering, University of New South Wales, Sydney, 2052, Australia. Email: chun.h.wang@unsw.edu.au
[b] Graduate School of Biomedical Engineering, University of New South Wales, Sydney, NSW 2052, Australia.
[c] Institute of Mechanical, Process and Energy Engineering, Heriot-Watt University, Edinburgh, EH14 4AS UK.
[d] The Robotics and Autonomous Systems Group, Commonwealth Scientific and Industrial Research Organization (CSIRO), Pullenvale, 4069, Australia.
†Electronic Supplementary Information (ESI) available: [details of any supplementary information available should be included here]. See DOI: 10.1039/x0xx00000x

detection range (50 to 200% strain) with a highly non-linear sensitivity (GFs varying from 57 to 1903). Thickness-gradient films for high GF and stretchable strain sensors have been first introduced by Liu et al. [46]. The sensors demonstrated highly variable GF depending on the applied strain: 161 for ε < 2%, 9.8 for 2% < ε < 15%, and 0.58 for ε > 15%. The strain sensors could withstand a uniaxial strain of more than 150%. Huang et al. [47] proposed a wrinkled-enabled, carbon black−Ecoflex based strain sensor, which exhibited large stretchability with a maximum recoverable strain of up to 500%, a high sensitivity of 68 in the strain range of 300−500%. More recently, Biang et al. [48] and Chu et al. [49] proposed a gradient wrinkle technique to further improve the performance of stretchable strain sensors. These strain sensors utilizing the wrinkle/thickness gradient technique exhibited super high GFs (maximum GF of 167665), and a broad strain range (up to 300-400%). However, these sensors showed high non-linear strain sensitivity/response, which complicates their use in real-world applications. Additionally, in these works, the micro-cracked films should remain uncoated for their effective sensing improvement, while this can lead to the delamination of sensing materials and poor durability of sensors over long-term loading cycles.

In this work, we present a thickness-engineering technique to create variable thickness (VT) sensors, which can be fabricated directly on 3D printed substrates. The spatial variation in the sensor thickness, in particular the inherent random irregularities in the sensor's thickness, traps microcracks within small regions of varying thickness, thus restricting the formation of long cracks during stretching. This mechanism endows the sensors with high stretchability and sensitivity while maintaining a highly linear response. Our technique entails the deposition of a thin film of PEDOT:PSS, which is reinforced by carbon nanofibers (CNFs), on the undulating surface of a 3D printed substrate. With a given 3D printing setting, the printed surface creates an alternating pattern of variable thickness film with some slight random irregularities. When stretched, the sensor layer fragments non-uniformly resulting in low-density, deep cracks in the thicker region and high-density, shallow microcracks in the thinner region. The sensing film is then coated by a covering TPU layer. Due to the thermoplastic nature of TPU, the coated layer would not penetrate into the PEDOT:PSS sensing film and thus not restrict the microcrack formation in there. The coated layer improved the mechanical resilience and durability of the sensor without compromising the sensing performance. Such a design gives rise to high stretchability and linear working range in the parallel-to-print direction while being insensitive to strain in the perpendicular direction. Experimental results show that the new sensor can undergo high strains without breaking ($\varepsilon_{\text{breakage}}$ (ε_b) ~ 160%) and exhibit high sensitivity with a GF of 151 and a linear strain range of ~ 97%. By changing the principle stretching direction from parallel to perpendicular to the printing direction, the PEDOT:PSS-CNF sensors change from being highly sensitive to insensitive to strain, hence the sensors show unidirectional strain sensing behaviour. To demonstrate the potential of the unidirectional sensors, we print and incorporate them into a soft glove to act as a master console to control a flexible and soft surgical robotic arm with an integrated surgical grasper. Results reveal that our sensors enable the soft glove to replace conventional and rigid master consoles that are currently being used in surgical robotic systems, providing better ergonomics for the surgeons with great comforts and intuitive control during operations.

2 Results and discussion

2.1 Design and fabrication of the VT sensors

The fabrication process of the VT strain sensors based on the thickness-engineered conductive films is schematically illustrated in Figure 1A. Briefly, a TPU substrate was 3D printed with a specific infill density (step one) to yield a periodic wavy structure parallel to the stretching direction. The infill density, presented in percentage, is defined as the ratio of the width of the printed tracks to the spacing between two neighbouring tracks [31]. The TPU substrate was then treated with oxygen plasma for 10 minutes to enhance the surface wettability and lower the contact angle, thus creating a more hydrophilic surface for quality coating of the sensor material (step two). A hybrid conductive solution made of PEDOT:PSS and CNFs was drop-cast, brushed, and dried overnight at room temperature on the top surface of the 3D printed TPU substrate, resulting in a thickness-engineered strain sensing film on the TPU substrate (step three). The 3D printed substrate automatically induced thickness variations in the PEDOT:PSS film, creating three thickness regions, namely, Region *I*, Regions *ii,* and Region *iii*. High-magnification schematics in step three show the three regions formed in the thin film sensor. The thicknesses of the three regions are denoted as t_i, t_{ii}, and t_{iii}, respectively. Finally, another TPU layer was 3D printed on top of the sensing layer to complete the fabrication of the sandwich-structured strain sensor (step four). The sandwich structure protects the sensing layer from direct exposure to the environment and enables the sensor to withstand large mechanical deformations [33].

Scanning electron microscope (SEM) images were taken to examine the morphology of the sensing layer without printing the top encapsulating TPU layer. Figure 1B depicts SEM images of a 3D printed TPU substrate coated with the PEDOT:PSS sensing film. As shown, in the case of 90% nominal infill printed TPU substrate, a periodic waveform structure with peaks and valleys was formed by the 3D printing process, with track height and width being around 300 and 400 μm, respectively. The PEDOT:PSS sensing layer was successfully deposited over the 3D printed TPU substrate with a highly smooth surface. No delamination and large cracks of the coated conductive film have been observed, revealing a good interfacial adhesion between PEDOT:PSS and TPU substrate. The magnified SEM images showed different thicknesses of the sensing layer at the peaks of the printed tracks (Region *iii*) and in the valleys between the tracks (Region *i*). These two thicknesses are measured to be approximately 2 μm (for Region *i*) and 40 nm (for Region *iii*). The interconnecting Region *ii*, which connects Regions *i* and *iii*, has a variable thickness, ranging from 40 nm to

2 μm. Three types of conductive materials were formulated to examine the effects of nano-reinforcements on the performance of the VT sensors: (a) 1wt% PEDOT:PSS solution, referred to as "PEDOT sensor", (b) 1wt% PEDOT:PSS solution containing 2 mg/ml CNF, referred to as "PEDOT-CNF sensor", and (c) 1wt% PEDOT:PSS solution containing 4 mg/ml CNF, referred to as "High-conc. PEDOT-CNF sensor". The electrical conductivities of these three materials have been measured to be 0.0737, 0.65, and 17.3 S/m, respectively. We drop-cast the same volume of content from these three materials. Therefore, the thickness of the sensing film is the same for all fabricated sensors.

2.2 Strain sensing performance

To explore the strain sensing performance of the thickness-engineered sensors in terms of GF, stretchability, and linearity, they were subjected to various dynamic mechanical loading while their electrical resistance was measured simultaneously (Figure S1A). Figure 2A gives the relative change of the resistance ($\Delta R/R_0$, where R_0 is the initial resistance of the sensor) versus the applied strain for a strain sensor when stretched to 50%. As shown, the resistance of the sensor gradually increased in the first stretching cycle and $\Delta R/R_0$ reached to the peak value of 31 at 50% strain. The peak electrical resistance of the 3D printed PEDOT sensor continued to increase in the first three cycles, shown in green, yellow, and blue colour in Figure S1C, and became stable and reversible at the 4th cycle and thereafter. We defined these initial cycles as pre-stretching training cycles to ensure the high-performance strain sensing behaviour of strain sensors. To further analyse the sensing performance, the GF of the strain sensor was calculated from the slope of the $\Delta R/R_0 - \varepsilon$ curve, i.e., $\Delta R/R_0$ divided by the applied strain (ε) ($GF = \Delta R/\varepsilon R_0$). As depicted in Figure 2A, after pre-stretching cycles, the 3D printed PEDOT sensor showed an ultra-high GF of around 417, significantly greater than that of the sensor before pre-stretching (*i.e.*, GF of 127 in the first cycle). These results show that pre-stretching training plays an important role in improving the sensors' strain sensing performance by initiating and stabilizing a microcrack network and by ensuring that all the microcracks are fully developed but not linked to form channel cracks. Therefore, hereafter, all the sensors in this study have been pre-stretched before the strain sensing tests to obtain their optimum sensing performance. The details of the pre-stretching experiments and results are brought in the Supplementary Section and Figure S1B-D. For comparison, electromechanical tests were also conducted on samples fabricated from flat TPU substrates with a uniform PEDOT:PSS film. As depicted in Figure 2A, the PEDOT sensor with a flat substrate initially started to crack at ε ~3% with a similar slope/GF to the pre-stretched VT sensor, but quickly experienced an electrical failure at the breakage strain, $\varepsilon_b \sim 7\%$. This behaviour is expected as large channel cracks quickly form in the flat sensor while, large cracks are contained in parallel islands throughout the width of the 3D printed sensor (Figure 2B). A sensor was considered broken where its resistance exceeded 100 MΩ with irreversible resistance change, i.e. the resistance value did not recover upon removing the strain. Because of this irreversible response to mechanical deformation, the flat PEDOT:PSS sensors therefore cannot be used as reliable stretchable strain sensors. In contrast, our thickness-engineered sensors offer reversible electromechanical performance under a significantly higher working strain range.

The morphology of the strain sensing layer during stretching helps to understand why thickness-engineered sensors have superior stretchability compared to the flat samples. The optical images in Figure 2B were taken from the top surface of the PEDOT:PSS film coated on both flat and 3D printed TPU substrates. When the flat substrate sample was stretched to 50% strain, channel-like microcracks were clearly observed causing its electrical failure at small strains. On the other hand, when the sensor with the 3D printed substrate was stretched to 50% strain, disconnected islands of smaller cracks (macro- and micro-cracks) were observed, enabling the PEDOT:PSS sensing film to withstand extremely large strains without losing the electrical conduction. As shown in Figure S2, once the strain was released, the generated crack edges were connected again, resulting in reversible changes in the electrical resistance.

The linear operation range denoted as ε_l, is defined as the strain up to which the linear regression coefficient R^2 exceeds 95% [33]. To enhance the sensors' linear operation range, CNF nanofillers were incorporated into PEDOT:PSS to bridge between microcrack edges and prevent the abrupt increase of the resistance. Two concentrations of CNFs in the PEDOT:PSS solution were formulated: a low concentration of CNFs, which is referred to as "PEDOT-CNF sensor", and a higher concentration of CNFs, denoted as "High-conc. PEDOT-CNF sensor". As shown in Figure 2C, the PEDOT sensor showed a breakage strain of $\varepsilon_b \sim 60\%$, while the PEDOT-CNF and high-conc. PEDOT-CNF sensors exhibited breakage strains of $\varepsilon_b \sim 110\%$ and $\sim 161\%$, respectively. In addition to the higher breakage strain, the linear operation ranges of the sensors are also greatly improved after the addition of CNFs. As shown in Figure S1E, the linear operation range increased significantly from $\varepsilon_l \sim 33\%$ for the PEDOT sensor to $\varepsilon_l \sim 61\%$ and $\sim 97\%$ for PEDOT-CNF and High-conc. PEDOT-CNF sensors, respectively. Although the addition of CNFs improved the stretchability and linearity of the sensor, it caused the linear GF to decrease from 417 for the PEDOT sensor to 282 and 151 for PEDOT-CNF and High-conc. PEDOT-CNF sensors, respectively. The GF dropped due to the CNFs preventing the PEDOT:PSS film from creating large cracks, especially in Region *ii*, by forming conductive bridges between the crack edges. However, these sensing parameters of our sensors are still remarkable compared to recently reported sensors as compared in Figure S3. The high magnification SEM image in Figure 2D shows how CNFs can improve the stretchability by bridging the opening of the microcracks in Region *ii* of a PEDOT-CNF sensor under 50% strain. It is noted that the CNFs were pulled out from the PEDOT:PSS matrix and crossed over the microcracks, i.e., restricting their opening and coalescence. This behavior increases the operation strain range by keeping the sensor's resistance low as well as improve the linearity of the sensor by

preventing abrupt changes in the electrical resistance upon stretching. The responses of a PEDOT-CNF sensor at six different peak strain levels, namely 50%, 30%, 20%, 10%, 5%, and 2% exhibit great linearity and minimal hysteresis (Figure 2E). Furthermore, the cyclic durability of a PEDOT-CNF sensor in Figure 2F shows a consistent response with great stability under repeated stretching with a 9.8% drift after 2500 cycles at 50% strain. A comparison of the performance of the current VT sensors with notable stretchable strain sensors reported in the literature so far is presented in Figure S3. The VT sensors demonstrate superior performance in terms of GF and linear operation range among all the sensors being considered.

The microcrack morphology in the PEDOT:PSS layer has been shown to have a direct relationship with the thickness of the layer. As evident from the optical images shown in Figure S4, the thicker the PEDOT:PSS layer is, the bigger the microcracks are. This is true for both 3D printed and flat substrates. The PEDOT sensors shown in Figures S4A, B, and C possess a layer thickness of ~ 42, 324, and 625 nm, respectively, based on the volume of the solution per unit flat area. Since the thickness of the PEDOT:PSS layer is variable on 3D printed substrates, an average thickness is assigned to them. The average thickness of the sensor on a 3D printed substrate is defined as the thickness of the sensing layer when the same volume of the material was coated on a flat substrate with the same geometry. Figure 3A illustrates the effect of PEDOT:PSS thickness on the GF and strain sensing range of strain sensors. Results show that the GF increases with the PEDOT:PSS thickness. However, the flat substrate samples (PEDOT:PSS thickness greater than 250 nm) stopped functioning when the strain reached 15% because their resistance exceeded 100 MΩ and upon unloading the resistance did not return to its initial value, indicating permanent damage. In contrast to the small sensing range of uniform thickness samples, the VT sensors printed on 3D printed substrate showed higher stretchability irrespective of their thicknesses. A sensor with an average PEDOT:PSS thickness of 625 nm showed a breakage strain of ~ 60%, significantly above the 7% breakage strain of the sensor with the same thickness printed on a flat TPU substrate.

To analyse the effect of infill density on the strain sensing performance, TPU substrates with different nominal printing densities in the top surface, ranging from 100% (overlapped) to 5% (which is equal to a single printing track on top of a 100% infill sublayer) were 3D printed as shown in Supplementary Figure S5. The PEDOT:PSS layer displayed different morphologies following the printing patterns of the substrates. The strain sensing characteristics of the PEDOT sensors with different infill densities and an averaged PEDOT:PSS thickness of 625 nm are compared in Figure 3B. The results reveal that the sensor with a 100% infill density exhibits the highest sensitivity (GF ~ 417). Starting from 100% infill density, which is the highest permissible setting of the printer, the GF decreases first when we decreased the infill density. This is corresponded to the increasing gap between the printed tracks. As the infill density goes below 40%, the PEDOT:PSS starts to follow the second/bottom printed TPU layer (the one below the top layer). This bottom TPU layer has an infill density of 100%, therefore the GF increases gradually when infill density is further decreased. It is also noted that the sensor with the lowest infill density, i.e. 5%, has similar sensitivity as that of the 100% infill sensor because it consists of a single printed track on a 100% infill density substrate (see Figure S5G).

2.3 Strain sensing mechanism

The VT sensors have a unique topology of spatially varying thickness that prevents the channelling and coalescence of microcracks. The non-uniform thickness with some randomness was achieved by utilizing 3D printing to fabricate a substrate with a desired surface undulation pattern with the printing direction being parallel to the direction of stretch. The undulations in the 3D printed surfaces gave rise to thickness variations in the resultant sensors made by casting liquid PEDOT:PSS solutions, with and without CNFs. When stretched, instead of forming through-width channelled cracks in the case of uniform PEDOT:PSS films (as shown in Figure 2B), non-continuous microcracks with different sizes were formed through the width of a VT sensor. The resultant sensor then contained PEDOT:PSS coating regions of small, medium, and large thicknesses. Larger cracks (longer and wider) formed in regions of greater thickness, shown as Region *i* in Figure 4A, while smaller (shorter and narrower) cracks formed in regions of lesser thickness, i.e. Regions *ii* and *iii*. The co-existence of these smaller (~ nanoscale) cracks next to the larger (~ micro- and macro-scale) cracks is the key to expanding the working range, i.e., stretchability. The smaller cracks, with inherent irregularities in spacing and length, prevent the microcracks from coalescing and channelling, thus keeping the electrical resistance within the measurement range. This phenomenon is illustrated in Figure 4B and the three-dimensional schematic of Figure 4C. Cracks formed in Region *i*, i.e., the largest cracks, spread into Region *ii* (medium thickness region) and eventually into Region *iii*, where the size of cracks are the smallest. The irregularities in the cracks, such as random crack tip positions and crack lengths, trapped the microcracks in Region *iii* and prevent them from linking with the microcracks in the adjacent Region *ii*. This localization or trapping of microcracks enables the sensor to withstand higher strains. Cracks initially formed in Region *i* are prevented from growing into adjacent Region *i* by thickness variations in middle Regions *ii* and *iii*. As the applied strain increases, the microcracks eventually connect and form long cracks (through the width of the sensor), causing the resistance of samples to exceed the measurement range, leading to electrical failure.

The electrical resistance of the sensor in parallel to the printing direction can be modelled as an equivalent circuit of three resistors "in parallel", repeated *n* times over the width of the sensor, where n denotes the number of valleys and peaks across the width of the sensor. This circuit analogy is shown in Figure 4A for a PEDOT sensor printed on a 90% infill substrate. The total resistance of the sensor, R_t, can be expressed in terms of the resistances of the three regions, i.e., R_i, R_{ii}, and R_{iii}, where the subscripts *i*, *ii*, and *iii* denotes quantities pertinent to Regions *i*, *ii*, and *iii*,

$$R_t = \frac{1}{\frac{n}{R_i} + \frac{n}{R_{ii}} + \frac{n}{R_{iii}}} \quad (1)$$

When the sensor is subjected to an applied strain ε, the electrical resistance of each region is related to their initial value and the respective GF, i.e., $R_i = R_{i,0}(1 + \varepsilon \times GF_i)$, $R_{ii} = R_{ii,0}(1 + \varepsilon \times GF_{ii})$, and $R_{iii} = R_{iii,0}(1 + \varepsilon \times GF_{iii})$, where the subscript 0 denotes the resistance pertinent to the initial, unstretched condition ($\varepsilon = 0$). As shown in Figure S2, the cracks created by the pre-stretching re-joined and the initial resistance ($R_{i,0}$) returned (approximately) to the original value. Therefore, $R_{i,0}$ is still much lower than $R_{iii,0}$ since the thickness of Region *i* is much larger than that of Region *iii*. As a result, $R_{i,0} \ll R_{ii,0} \ll R_{iii,0}$. Therefore, the total initial resistance of the three parallel resistors is well approximated by $R_{t,0} \sim R_{i,0}/n$. Under large strains, as shown in the SEM Figure 4A and schematic Figure 4C, channel cracks form in Regions *i* and *ii*, causing their resistance to rapidly exceed the measurement range at a very small strain, around 5% ($R_i, R_{ii} \rightarrow \infty$), whereas Region *iii* maintains its resistance. Therefore, the total resistance under strains greater than 5% can be simplified as below:

$$R_t \sim \frac{R_{iii}}{n} \quad (2)$$

As a result, the overall GF of the sensor in the parallel direction ($GF_{t,par}$) can be derived using this circuit analogy as below:

$$GF_{t,par} = \frac{\Delta R_t}{\varepsilon R_{t,0}} \sim \frac{R_{iii} - R_{i,0}}{\varepsilon R_{i,0}} \gg GF_{iii} \quad (3)$$

Since $R_{i,0} \ll R_{iii,0}$, the total GF of the sensor in the parallel direction is therefore much greater than that of Region *iii*.

While the VT sensor offers the highest strain sensitivity in the stretching direction parallel to the printing direction, it shows very small strain sensitivity in the stretching direction perpendicular to the printing direction. Therefore, the VT sensor would serve as an excellent unidirectional strain sensor. The strain sensitivity performance of the VT sensor in parallel and perpendicular to the printing directions are compared in Figure 5A. A more magnified graph in Figure S6 shows the resistance change of the VT sensor when stretched perpendicular to the printing direction, revealing the GF of only ~ 0.2 in this direction. This excellent feature of unidirectional strain sensitivity makes it possible to use this sensor in applications where the main interest is the deformation/strain in a certain direction. Figure 5B illustrates a SEM image of the VT sensor under stretch perpendicular to the printing direction. Similar to the stretching in the parallel direction, three thickness regions, namely *i*, *ii* and *iii* are formed upon stretching in here, and only Region *i* undergoes major cracking, while Regions *ii* and *iii* experience minimal cracking. The 3D printed tracks were designed in a wavy shape (Figure 5C and D) to minimize the fragmentation of the PEDOT:PSS layer on the tracks. The high magnification SEM images in Figure 5C illustrate the formation of microcracks on the curved section of the printed tracks and the different crack morphologies that exist in the valleys and on the curved end of printed tracks. The curved ends of the printed tracks provide conductive pathways even under high strain levels (ε ≥ 50%). Only small microcracks form on the curved sections of the printed tracks in Regions *ii* and *iii*, but these do not coalescence into channel cracks even at 50% strain. The absence of large cracks along these regions is the main reason for the insensitivity of sensors to the strain applied perpendicular to the printing direction.

The behaviour of the sensor perpendicular to the printing direction can be modelled as periodic resistors "in series"; the equivalent circuit model is shown in Figure 5B. Given the fact that $R_{i,0} \ll R_{ii,0} \ll R_{iii,0}$, the overall resistance and GF can be estimated as below for the three resistors in series:

$$R_{t,0} = n(R_{i,0} + R_{ii,0} + R_{iii,0}) \sim n\, R_{iii,0} \quad (4)$$

As shown in the SEM Figure 5B and schematic Figure 5D, when the sensor is stretched in the perpendicular direction, the resistance of Region *i* increase rapidly with strain to exceed the measurement range due to the formation of channel cracks. However, Regions *ii* and *iii* and the curved areas (shown in Figure 5D) remain intact and maintain conductance. The total resistance under strain can therefore be simplified as below:

$$R_t = n(R_{iii} + R_{ii}) \quad (5)$$

And the total GF can be calculated as below:

$$GF_{t,per} = \frac{\Delta R_t}{\varepsilon R_{t,0}} \sim \frac{n(R_{iii} + R_{ii}) - nR_{iii,0}}{\varepsilon n R_{iii,0}} = \frac{(R_{iii} + R_{ii}) - R_{iii,0}}{\varepsilon R_{iii,0}} \sim k_{iii} \ll GF_{t,par} \quad (6)$$

This proves the GF in the perpendicular direction is close to that of Region *iii,* and considerably lower than that of the sensor in the parallel direction.

2.4 Application demonstration

The excellent features of the developed VT sensors offer great potential for the remote control of soft machines with a hand gesture or human joint/body motion. Most surgical robotic systems utilize a master-slave interface to operate where the surgeons remotely control the flexible surgical arm to cut target tissues *via* the master side that captures the surgeons' hand motions [41]. Existing master consoles use rigid components such as encoders in the form of a graspable or holdable structure to mimic the surgeons' wrist motions and then send commands to the motor housing to control flexible surgical tools inside the patient body. However, the use of rigid structures causes discomfort and poor ergonomics to the

surgeons. There is currently a need for a soft master console that is lightweight and can conform to the user's hand while offering great comfort and ease of control. To bridge the gap in the flexible master console for surgical systems, we developed a VT sensors-based soft glove that can precisely mimic the hand motion for the control of a soft robotic catheter that is driven by a hydraulic Soft Microtubule Artificial Muscle (SMAM) [42] and tendon-sheath mechanism. The robotic catheter consists of a soft robotic arm with an integrated gripper. The overall structure of the soft robotic catheters is shown in Figure 6A. The catheter has a diameter of 4.15 mm. The control flow of the robotic catheter is shown in Figure S7. To control the bending and gripping motions of the flexible robotic catheter, the sensors built into the soft glove provide motion signals, which precisely map the user's wrist and finger bending motion. In particular, to create a gripping motion, surgical forceps inspired by Da Vinci surgical robotic system were 3D printed and then integrated into the tip of the cut-out tube. The forceps are actuated by a tendon-sheath mechanism from Asahi Intecc Co. The forceps close the grip when the tendon is pulled and open the grip by a rubber string when the tension in the tendon drops (Figure 6B). To induce bending motion for the flexible arm, we created asymmetric and triangular cut-outs in a polytetrafluoroethylene (PTFE) tube with a sharp knife, turning the tube into a bending element that could be actuated by a fluid-driven soft artificial SMAM. To achieve desired motions, the SMAM was firstly elongated to 50% of its original length under fluid (water) pressure generated by a syringe located remotely via a hydraulic transmission tube routed inside the catheter body. By increasing the elongation of SMAM, the device could generate a stronger pulling force against the load when bending. The proximal end of the muscle was then fixed to a 3D printed base where its distal end was attached to the end of the cut-out PTFE tube. Once the hydraulic pressure increases, the SMAM elongates and forces the cut-out tube to bend towards the opposite side, i.e. upward (Figure 6B). And when the hydraulic pressure in the SMAM drops, it becomes shorter compared to its initial length and makes the cut-out tube bend downward (Figure 6B). Compared to the surgical robots presented in [43, 44], the current design shows a better capability with two-way bending motions; the surgical robots reported in the literature so far using the cut-out tube design are not capable of two-way bending motion [42].

To provide the desired signals for controlling the flexible surgical arm, two VT sensors were attached to a fabric glove on the wrist location and the metacarpophalangeal joint of the index finger. The bending angles at these two locations were determined in real-time from the resistance changes, which were then used as commands to control the length of SMAM and the tension in the tendon. As a result, the wrist sensor can control the movement of the robotic catheter/tentacle and the finger joint sensor control the movement of forceps/gripper. Our proof-of-concept prototype is shown in Figure 6C. Several experiments were carried out to examine the bending and gripping capability of the catheter under the control of the two VT sensors (Figures 6D). The soft tentacle could successfully follow the wrist movement with high precision as shown in Figure 6E (99% matching motion for a bending angle between -20 and 40 degrees). The tendon-sheath mechanism could control the forceps to open, half-grip, and grip (Figure 6F). A comparison of the gripper angle and finger joint's angle is presented in Figure 6G. The gripper could match the finger's movement with a 95% accuracy. Furthermore, as shown in Figures 6H and Movie S1, the robotic catheter could bend (/wrist down), grip, lift and drop an object at any angle based on a signal from the VT sensors for desired applications, indicating that the developed robotic catheter equipped with the VT sensor can be used in surgical procedures. The real-time response of the wrist and finger joint sensors corresponding to the motions shown in Figure 6H, reveals the response time of the sensor is a few seconds and the recovery time is less than 12 seconds (Figure 6I).

3 Conclusion

In this paper, we have demonstrated a new sensor design based on spatially-varying thickness to prevent the formation of channel cracks and thus greatly increase the working range and linearity of flexible sensors. The sensors have been made on 3D printed TPU substrates to provide a variable surface pattern, although the technique is also applicable to other materials and substrates. 3D printing also provides the versatility to tailor the properties of the sensors by adjusting printing parameters such as printing direction and infill density. The variable thickness thin-film strain sensors have been made by drop-coating a conductive film on 3D printed surfaces. The infill density of the substrate affects the thickness gradient and alters the sensitivity of the sensor, while the angle between the printing direction with the stretching direction affects the anisotropy of the sensing layer: a parallel print gives the highest sensitivity whereas a perpendicular print gives an insensitive strain sensor. [31]. As a result, highly stretchable, unidirectional strain sensors fabricated on a 100% infill density substrate were capable of a high strain sensitivity (GF ~ 417) and a linear operating range of up to 33% strain. The novel VT sensors exhibited a highly anisotropic piezoresistive response to deformation, forming sensors of high strain sensitivity on printed surfaces along the stretching direction. By introducing nanofibers into the VT sensor layer, a considerably higher linear working range of 97% strain was achieved through bridging the microcracks. The current VT sensors have a superior performance compared to notable stretchable strain sensors reported in the literature so far (Figure S3).

The current sensors enable precision motion sensing and control of subtle to large deformations in soft bodies. To demonstrate the performance of our sensors in a real-life application, we constructed a master-slave soft surgical system using VT sensors-based glove as a soft master console to control a novel SMAM-driven soft surgical tentacle gripper that can bend in two opposing directions. The soft catheter could successfully follow the wide range of motions of the soft glove with high accuracy of 99% to accomplish the desired manipulation of a surgical task including bending motion and

gripping soft objects using human hand gestures. This research paves the way for low-cost and widely accessible 3D printing techniques to fabricate highly sensitive and stretchable sensors that can be readily integrated into 3D printed soft robots and human-machine interfaces, thus creating new possibilities and opportunities for multifunctional intelligent soft machines, particularly in the field of robotic surgery.

Experimental Details

Materials

PEDOT:PSS aqueous solution with a concentration of 1.1wt% was purchased from Heraeus Deutschland GmbH. Carbon nanofibers were purchased from Pyrograf-III, grade PR-24-XT-HHT. TPU Ninjaflex filament was purchased from Thinglab Australia. The silver paste was purchased from SPI Supplies. All the chemicals were used as received.

Fabrication of the sensors

PEDOT:PSS aqueous solutions with different concentrations (1wt%, 0.5wt%, 0.25wt% and 0.125wt%) were prepared by diluting the base PEDOT:PSS solution (1.3 wt%, PEDOT:PSS=5:8) with DI water. PEDOT:PSS-CNF aqueous solutions were prepared by mixing CNFs and PEDOT:PSS solution with different mass ratios of CNFs. All the solutions were sonicated using a sonicator bath (Unisonics Australia Pty Ltd) for 3 hours at room temperature to obtain a homogenous solution. To fabricate the VT sensors, first, a substrate TPU with a thickness of 1 mm was 3D printed using Ninjaflex filament and a 3D-Gence One FDM printer. The surface of this substrate was designed to contain a slot in the shape of the sensing layer. The details of printing parameters used for 3D printing TPU are shown in Table S1. "Simplify3D" software was used to convert the CAD files to g-code format. After printing the substrate, it was detached from the printer's bed and placed inside the O_2 plasma cleaner (Harrick, PDC-002) for 10 minutes for surface treatment. After surface treatment, sensor solutions were drop-cast with specific volumes using a micropipette and then bushed on the TPU substrate using a Renoir nylon round craft paintbrush - size 6 (from Bunnings Australia). Afterward, it was kept at room temperature for 12 hours to get rid of all the water. Finally, it was placed on the printer's bed and a thin layer of TPU with a thickness of 400 microns was printed on top of the substrate to make the sandwiched sensor structure.

The flat sensors were fabricated on smooth TPU substrates by first 3D printing a TPU substrate on a glass plate, which was taped on top of the printer's ceramic bed. The bottom surface of the printed TPUs was then used as the flat substrate for creating flat PEDOT sensors. The thickness of the sensor layers on the flat TPU substrate was calculated by dividing the volume of the material used by the surface area. For 3D printed substrates, the average thickness was considered.

Characterization and strain sensing performance of the sensors

The morphologies of the sensors were characterized using a NanoSEM 230 field-emission scanning electron microscope (FE-SEM) with an accelerating voltage of 3.0 kV. The specimens that contained TPU on the top surface were sputter-coated with a layer of platinum (thickness = 15 nm). Optical micrographs were taken with a ZEISS Axio Zoom V16 microscope. The schematics were drawn using Solidworks 2020 software. The electrical conductivity of the sensors has been measured using an Ossila Four-Point Probe. An Instron 3369 machine was used for all of the tensile strain sensing tests. For tensile tests, two wooden strips were bonded to one side of the sensors using the superglue and the strips were clamped to the Instron machine as shown in Figure S1. For wire bonding, copper wires were attached to the sensors' surface using silver paste and then covered with aluminum tape. A Keysight 34465A digital multimeter was used to acquire the sensors' electrical resistance.

Controlling the soft catheter

The forceps were actuated by a tendon-sheath mechanism from Asahi Intecc Co. The tendon-sheath actuator comprised a Teflon coated wire tendon with a diameter of 0.27 mm and a round wire coil sheath with an inner diameter of 0.36 mm and an outer diameter of 0.8 mm which travels along the catheter body. A DC motor (Faulhaber, Germany) and a linear ball screw mechanism (MISUMI, Japan) were used to drive the tendon-sheath system. Two VT sensors were attached to a fabric glove at the wrist joint and the metacarpophalangeal joint of the index finger and measure the bending angle at these two locations based on its resistance change. A data acquisition device (QPIDe, Quanser, Canada) and MATLAB Simulink (Mathworks Inc., USA) was used to decode the electronic signals generated from the two VT sensors and the signals were filtered by a digital bandpass filter to reduce unwanted noise. Then, the signals were regulated by two simple PID controllers for the movement of each element of the robotic catheter (Supplementary Figure S7); the commands control the length of SMAM and the tension in the tendon. All parameters in two PID controllers were optimized based on experiments to provide smooth and stable movements with position errors less than 0.01 mm. Therefore, each resistance value in each force sensor corresponds to the bending angle of the robotic catheter and the state of forceps respectively.

Conflict of Interest

The authors declare no financial/commercial conflict of interest.

Acknowledgments

S.M. acknowledges the financial support provided to him by UNSW and CSIRO through an Australian Government Research Training Program (RTP) Scholarship (RSRA4088) and a Ph.D. top-up scholarship (RSRT4015), respectively. Scholarship RSRT4015 was funded by CSIRO's Active Integrated Matter Future Science Platform. The authors would like to thank Ms. Yuyan Yu for

assistance with the oxygen plasma surface treatment instrument.

Author Contributions

S.M. initialized the concept; designed and fabricated the sensors; designed and conducted the experiments; analysed the data and wrote the draft manuscript. M.T.T. and T.N.D. designed and fabricated the soft robotic catheter. M.A. wrote and revised the manuscript. D.H. supervised the work, wrote, and revised the manuscript. S.P. provided the PEDOT:PSS material and participated in the intellectual discussions. C.H.W. jointly initialized the concept, designed the experiments, supervised the work, and wrote and revised the manuscript.

References

[1] R. L. Truby, M. Wehner, A. K. Grosskopf, D. M. Vogt, S. G. M. Uzel, R. J. Wood, J. A. Lewis, *Adv Mater* **2018**, 30.
[2] T. Jin, Z. D. Sun, L. Li, Q. Zhang, M. L. Zhu, Z. X. Zhang, G. J. Yuan, T. Chen, Y. Z. Tian, X. Y. Hou, C. Lee, *Nat Commun* **2020**, 11.
[3] B. Ward-Cherrier, N. Pestell, L. Cramphorn, B. Winstone, M. E. Giannaccini, J. Rossiter, N. F. Lepora, *Soft Robot* **2018**, 5, 216.
[4] M. L. Hammock, A. Chortos, B. C. K. Tee, J. B. H. Tok, Z. A. Bao, *Adv Mater* **2013**, 25, 5997.
[5] A. Chortos, J. Liu, Z. A. Bao, *Nat Mater* **2016**, 15, 937.
[6] G. S. Fischer, T. Akinbiyi, S. Saha, J. Zand, M. Talamini, M. Marohn, R. Taylor, *P Ieee Ras-Embs Int* **2006**, 989.
[7] M. Abayazid, R. J. Roesthuis, R. Reilink, S. Misra, *Ieee T Robot* **2013**, 29, 542.
[8] S. B. Kesner, R. D. Howe, *IEEE Int Conf Robot Autom* **2010**, 2010, 1059.
[9] S. B. Kesner, R. D. Howe, *Int J Robot Res* **2014**, 33, 631.
[10] Z. Y. Liu, D. P. Qi, P. Z. Guo, Y. Liu, B. W. Zhu, H. Yang, Y. Q. Liu, B. Li, C. G. Zhang, J. C. Yu, B. Liedberg, X. D. Chen, *Adv Mater* **2015**, 27, 6230.
[11] D. X. Qiu, Y. C. Chu, H. X. Zeng, H. H. Xu, G. Dan, *Acs Appl Mater Inter* **2019**, 11, 37035.
[12] N. S. Lu, C. Lu, S. X. Yang, J. Rogers, *Adv Funct Mater* **2012**, 22, 4044.
[13] L. H. Li, H. Y. Xiang, Y. Xiong, H. Zhao, Y. Y. Bai, S. Q. Wang, F. Q. Sun, M. M. Hao, L. Liu, T. Li, Z. H. Peng, J. Q. Xu, T. Zhang, *Adv Sci* **2018**, 5.
[14] M. Amjadi, A. Pichitpajongkit, S. Lee, S. Ryu, I. Park, *Acs Nano* **2014**, 8, 5154.
[15] P. Wang, W. D. Wei, Z. Q. Li, W. Duan, H. L. Han, Q. Xie, *J Mater Chem A* **2020**, 8, 3509.
[16] J. J. Park, W. J. Hyun, S. C. Mun, Y. T. Park, O. O. Park, *Acs Appl Mater Inter* **2015**, 7, 6317.
[17] S. Y. Wu, S. H. Peng, Z. J. Han, H. W. Zhu, C. H. Wang, *Acs Appl Mater Inter* **2018**, 10, 36312.
[18] Z. H. Zeng, S. I. S. Shahabadi, B. Y. Che, Y. F. Zhang, C. Y. Zhao, X. H. Lu, *Nanoscale* **2017**, 9, 17396.
[19] C. Y. Yan, J. X. Wang, W. B. Kang, M. Q. Cui, X. Wang, C. Y. Foo, K. J. Chee, P. S. Lee, *Adv Mater* **2014**, 26, 2022.
[20] Y. N. Yang, Z. R. Cao, P. He, L. J. Shi, G. Q. Ding, R. R. Wang, J. Sun, *Nano Energy* **2019**, 66.
[21] J. Zhao, C. L. He, R. Yang, Z. W. Shi, M. Cheng, W. Yang, G. B. Xie, D. M. Wang, D. X. Shi, G. Y. Zhang, *Appl Phys Lett* **2012**, 101.
[22] J. H. Lee, J. Kim, D. Liu, F. M. Guo, X. Shen, Q. B. Zheng, S. Jeon, J. K. Kim, *Adv Funct Mater* **2019**, 29.
[23] Y. Liu, X. L. Shi, S. R. Liu, H. P. Li, H. L. Zhang, C. H. Wang, J. J. Liang, Y. S. Chen, *Nano Energy* **2019**, 63.
[24] M. D. Ho, Y. Ling, L. W. Yap, Y. Wang, D. Dong, Y. Zhao, W. Cheng, *Adv Funct Mater* **2017**, 27.
[25] T. T. Yang, W. Wang, H. Z. Zhang, X. M. Li, J. D. Shi, Y. J. He, Q. S. Zheng, Z. H. Li, H. W. Zhu, *Acs Nano* **2015**, 9, 10867.
[26] S. Y. Wu, R. B. Ladani, J. Zhang, K. Ghorbani, X. H. Zhang, A. P. Mouritz, A. J. Kinloch, C. H. Wang, *Acs Appl Mater Inter* **2016**, 8, 24853.
[27] S. Mousavi, P. Blanloeuil, T. Vinoth, D. Howard, C. H. Wang, *Materials Research Proceedings* **2021**, 18, 272.
[28] S. Pan, Z. Liu, M. Wang, Y. Jiang, Y. Luo, C. Wan, D. Qi, C. Wang, X. Ge, X. Chen, *Adv Mater* **2019**, 31, e1903130.
[29] J. H. Pu, X. Zhao, X. J. Zha, L. Bai, K. Ke, R. Y. Bao, Z. Y. Liu, M. B. Yang, W. Yang, *J Mater Chem A* **2019**, 7, 15913.
[30] X. W. Fu, Z. M. Liao, J. X. Zhou, Y. B. Zhou, H. C. Wu, R. Zhang, G. Y. Jing, J. Xu, X. S. Wu, W. L. Guo, D. P. Yu, *Appl Phys Lett* **2011**, 99.
[31] S. Mousavi, D. Howard, F. Zhang, J. Leng, C. H. Wang, *ACS Appl Mater Interfaces* **2020**, 12, 15631.
[32] O. A. Araromi, M. A. Graule, K. L. Dorsey, S. Castellanos, J. R. Foster, W. H. Hsu, A. E. Passy, J. J. Vlassak, J. C. Weaver, C. J. Walsh, R. J. Wood, *Nature* **2020**, 587, 219.
[33] S. H. Peng, S. Y. Wu, Y. Y. Yu, P. Blanloeuil, C. H. Wang, *J Mater Chem A* **2020**, 8, 20531.
[34] H. L. Sun, K. Dai, W. Zhai, Y. J. Zhou, J. W. Li, G. Q. Zheng, B. Li, C. T. Liu, C. Y. Shen, *Acs Appl Mater Inter* **2019**, 11, 36052.
[35] Q. Liu, J. Chen, Y. R. Li, G. Q. Shi, *Acs Nano* **2016**, 10, 7901.
[36] J. Lee, S. Shin, S. Lee, J. Song, S. Kang, H. Han, S. Kim, S. Kim, J. Seo, D. Kim, T. Lee, *Acs Nano* **2018**, 12, 4259.
[37] Z. Y. Liu, D. P. Qi, P. Z. Guo, Y. Liu, B. W. Zhu, H. Yang, Y. Q. Liu, B. Li, C. G. Zhang, J. C. Yu, B. Liedberg, X. D. Chen, *Adv Mater* **2015**, 27, 6230.
[38] Y. Y. Yu, S. H. Peng, P. Blanloeuil, S. Y. Wu, C. H. Wang, *Acs Appl Mater Inter* **2020**, 12, 36578.
[39] Y. R. Jeong, H. Park, S. W. Jin, S. Y. Hong, S. S. Lee, J. S. Ha, *Adv Funct Mater* **2015**, 25, 4228.
[40] Q. Liu, M. Zhang, L. Huang, Y. R. Li, J. Chen, C. Li, G. Q. Shi, *Acs Nano* **2015**, 9, 12320.
[41] M. T. Thai, P. T. Phan, T. T. Hoang, S. Wong, N. H. Lovell, T. N. Do, *Advanced Intelligent Systems* **2020**, 2, 1900138.
[42] P. T. Phan, M. T. Thai, T. T. Hoang, N. H. Lovell, T. N. Do, *Ieee Access* **2020**, 8, 226637.
[43] P. A. York, P. J. Swaney, H. B. Gilbert, R. J. Webster, *Ieee Int Conf Robot* **2015**, 1776.
[44] J. Gafford, M. Freeman, L. Fichera, J. Noble, R. Labadie, R. J. Webster, *Ann Biomed Eng* **2021**, 49, 219.
[45] Zhou, K. K., W. J. H. Xu, Y. F. Yu, W. Zhai, Z. Q. Yuan, K. Dai,

G. Q. Zheng, L. W. Mi, C. F. Pan, C. T. Liu, C. Y. Shen, *Small* **2021**, 17, 2100542

[46] Z. Liu, D. Qi, P. Guo, Y. Liu, B. Zhu, H. Yang, Y. Liu, B. Li, C. Zhang, J. Yu, B. Liedberg and X. Chen, *Adv. Mater.* **2015**, 27: 6230-6237.

[47] J. Huang, J. Zhou, Y. Luo, G. Yan, Y. Liu, Y. Shen, Y. Xu, H. Li, L. Yan, G. Zhang, Y. Fu, and H. Duan, *ACS Applied Materials & Interfaces* **2020** *12* (38), 43009-43017

[48] Z. Chu, W. Jiao, J. Li, H. Guo, Y. Zheng, R. Wang, X. He, *Chemical Engineering Journal*, **2021** 421, 1, 129873.

[49] Z. Chu, W. Jiao, Y. Huang, Y. Zheng, R. Wang, X. He, *Journal of Materials Chemistry A* **2021,** *9* (15), 9634-9643.

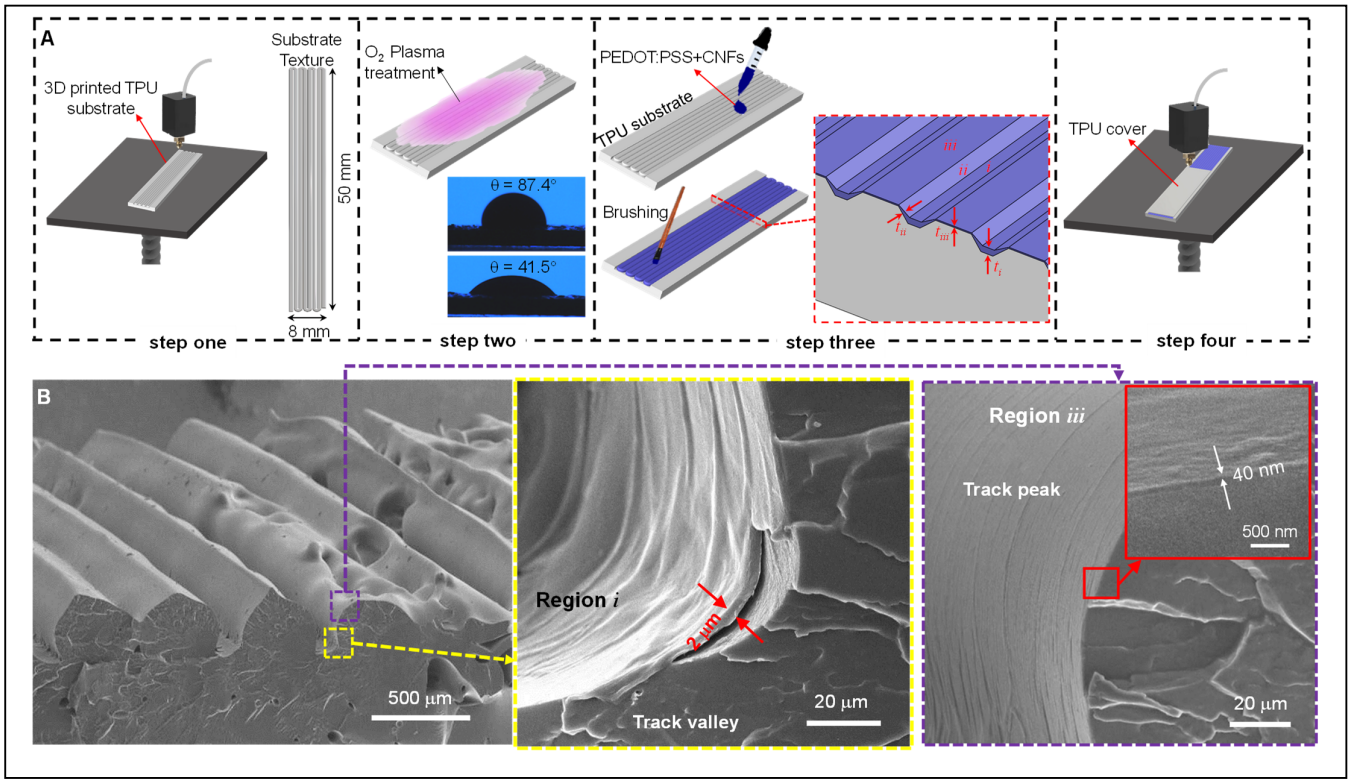

Figure 1. Fabrication process of the VT sensors. (**A**) In step one, the TPU filament is 3D printed to create the sensor substrates with a parallel texture and curved ends. In step two, the substrate is treated using oxygen plasma to achieve a hydrophilic surface, leading to an improvement in the wettability of the surface which subsequently reduces the water droplet contact angle on the TPU surface from 87.4° to 41.5°. At the next step, the PEDOT:PSS-CNF hybrid aqueous solution is drop cast and brushed onto the plasma-treated TPU substrate. The substrates with different infill densities create sensor layers with different variable thicknesses. The magnified image shows a model of the sensor layer's morphology. Three thickness regimes are formed due to the surface pattern of the 3D printed substrate, which are named Regions *i*, *ii*, and *iii*, and the corresponding thicknesses for these regions are shown as t_i, $t_{ii,}$ and t_{iii}, respectively. At the fourth and final step, a covering TPU skin is printed on top of the sensing material for physical protection. (**B**) The cross-sectional SEM of the PEDOT:PSS coating layer on a 90% infill TPU substrate shows different thicknesses on the printed track and in the valley between the tracks. The thickness of the sensor layer is measured to be around 40 nm and 2 μm in Regions *iii* and *i*, respectively.

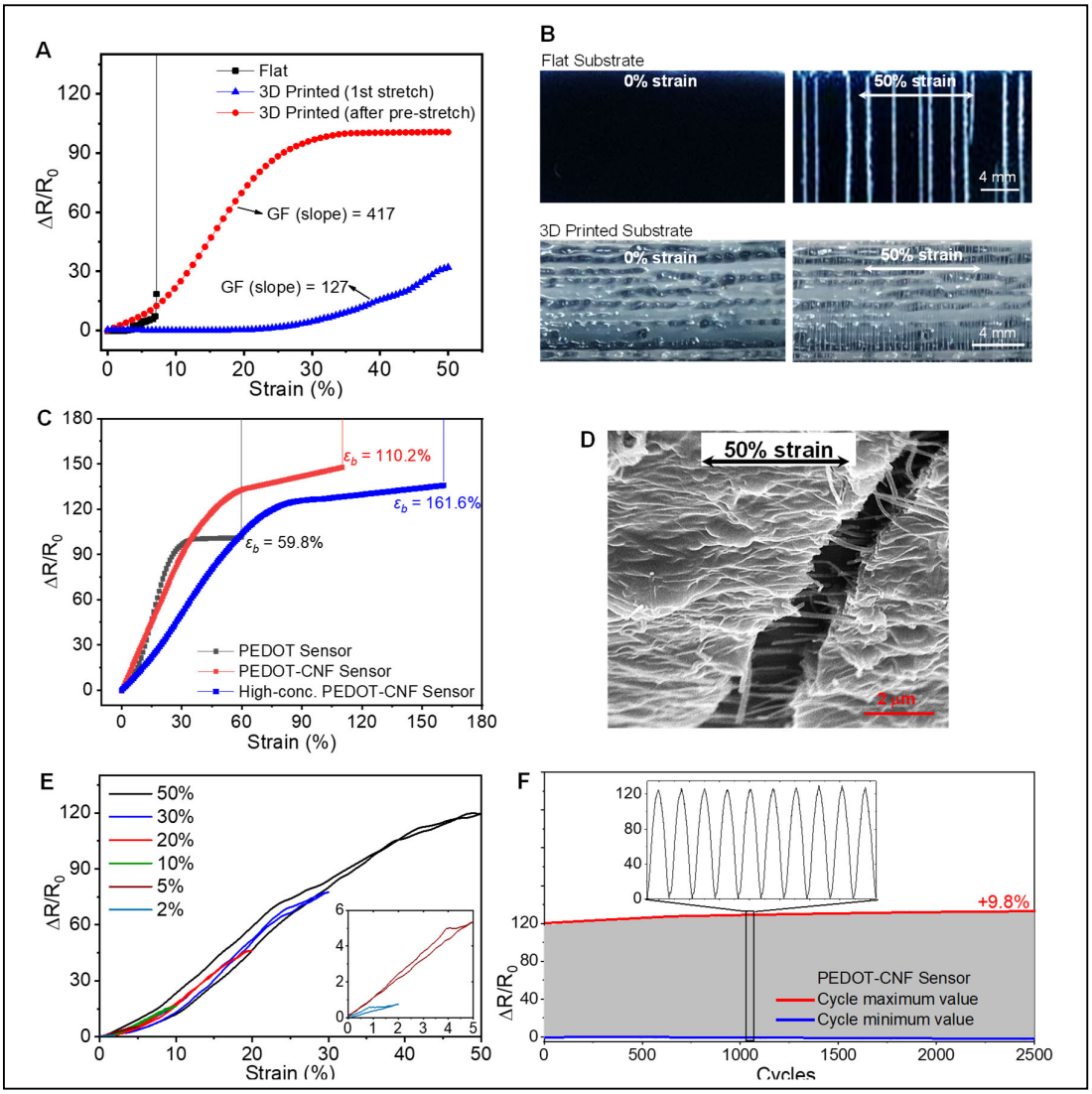

Figure 2. Electromechanical performance and characterization of the VT sensors. (**A**) The performance comparison for PEDOT sensors on flat substrates versus on 3D printed substrate. The graph compares the linear gauge factor and stretchability. (**B**) Optical images of the PEDOT sensors on the flat and 3D printed TPU substrates, demonstrating the microcrack morphology under 50% strain. (**C**) Resistance change versus strain for PEDOT, PEDOT-CNF, and High-conc. PEDOT-CNF sensors. (**D**) SEM image of PEDOT-CNF sensor layer showing the PEDOT:PSS-nanofibers network at 50% strain. The nanofibers are bridging a microcrack in Region *ii*. (**E**) The cyclic resistance change of the PEDOT-CNF sensor for different strain levels, from 2% up to 50%. The inset graph shows the resistance change for 5% and 2% strains. (**F**) Cyclic strain sensing performance of the PEDOT-CNF sensor under 50% tensile strains. The resistance drift is shown in red (9.8% after 2500 cycles).

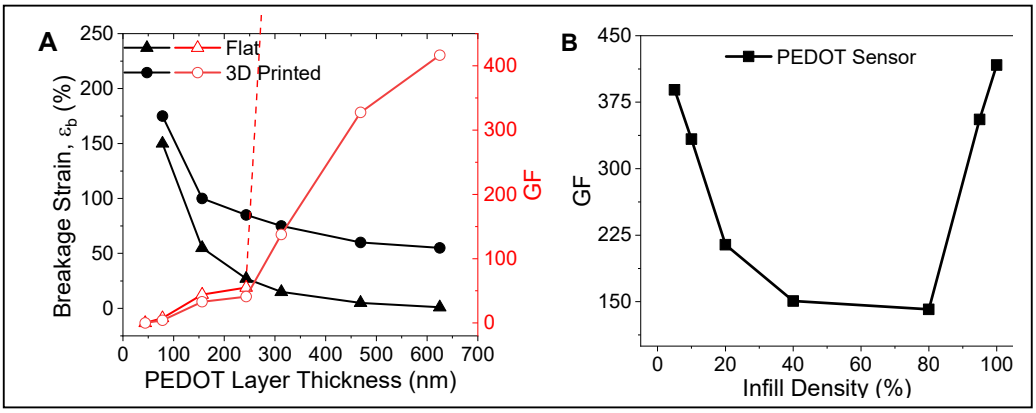

Figure 3. Analysis of sensor layer thickness and substrate infill density. (A) The effect of sensor layer thickness on strain sensing performance (GF and breakage strain) of the PEDOT sensors on the flat and 3D printed substrates. (B) The effect of substrate infill density on the GF of the PEDOT sensor.

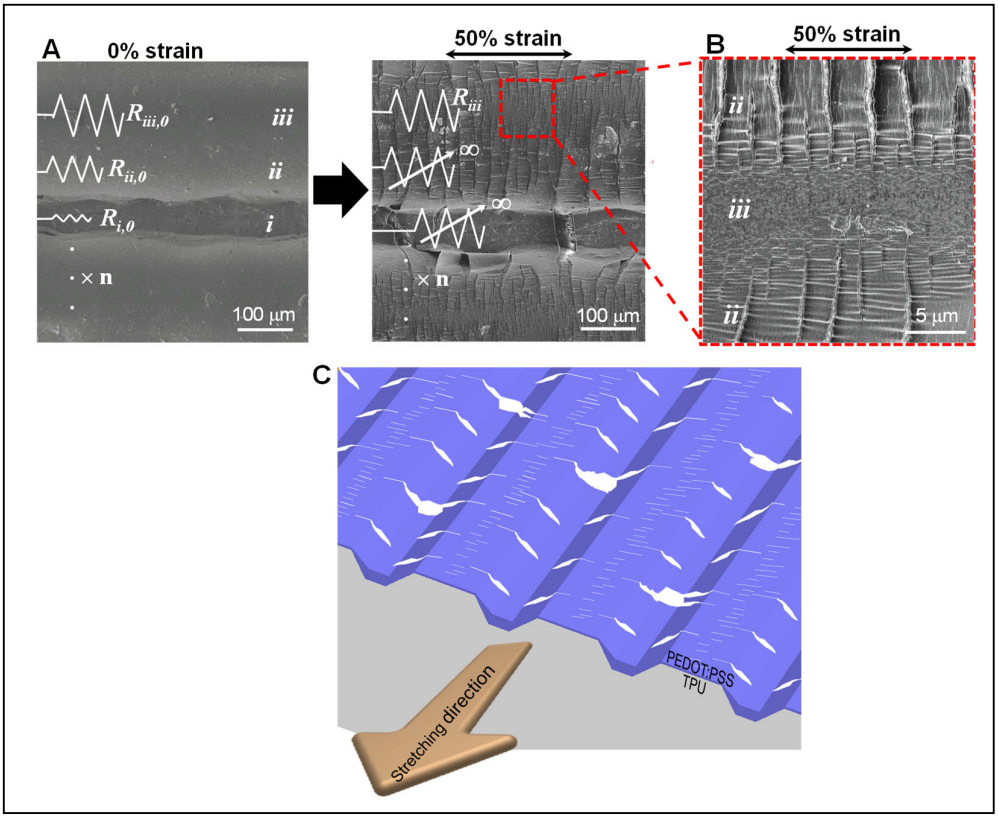

Figure 4. Operation mechanism of the VT strain sensor. (**A**) SEM images of the PEDOT sensor, showing the circuit analogy before and after being stretched for 50%. The resistance in the three regions increases unequally; *Ri* increases the most and goes overload. (**B**) magnified SEM image of the PEDOT sensor showing Regions *iii* and *ii* at 50% strain. (**C**) The three-dimensional schematic of the VT sensor illustrating the microcrack modelling of PEDOT:PSS variable thickness layer on TPU substrate. Once the VT sensor is stretched, three crack regions are formed, namely *i, ii,* and *iii*. Region *iii* act as a crack-trap, containing the large cracks, which were initially formed in region *i*.

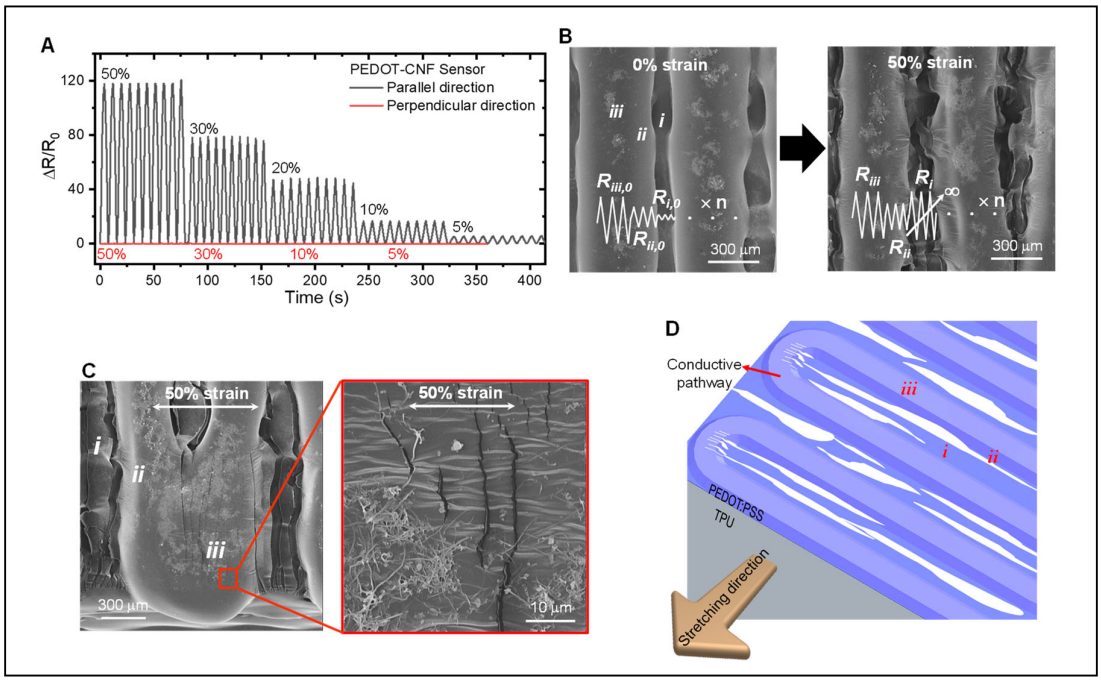

Figure 5. The unidirectional behaviour of the VT sensor. (**A**) The strain sensitivity of the PEDOT-CNF sensor for different strain levels in parallel (black) and perpendicular (red) to the printing direction. (**B**) SEM images of the PEDOT-CNF sensor, showing the circuit analogy before and after being stretched for 50% perpendicular to the printing direction. The resistance in the three regions increases unequally; R_i increases the most and goes overload. (**C**) Once the VT sensor is stretched perpendicular to the printing direction, the largest cracks are formed in Region *i*, while smaller cracks are formed in Regions *ii* and *iii* mostly at two ends (curved area), therefore Region *iii* can provide a conductive pathway even in high strains. The magnified image shows the cracks formed in region *iii* at 50% strain. **(D**) The three-dimensional schematic of the VT sensor illustrating the microcrack morphology of PEDOT:PSS variable thickness layer on TPU substrate when stretched perpendicular to the printing direction.

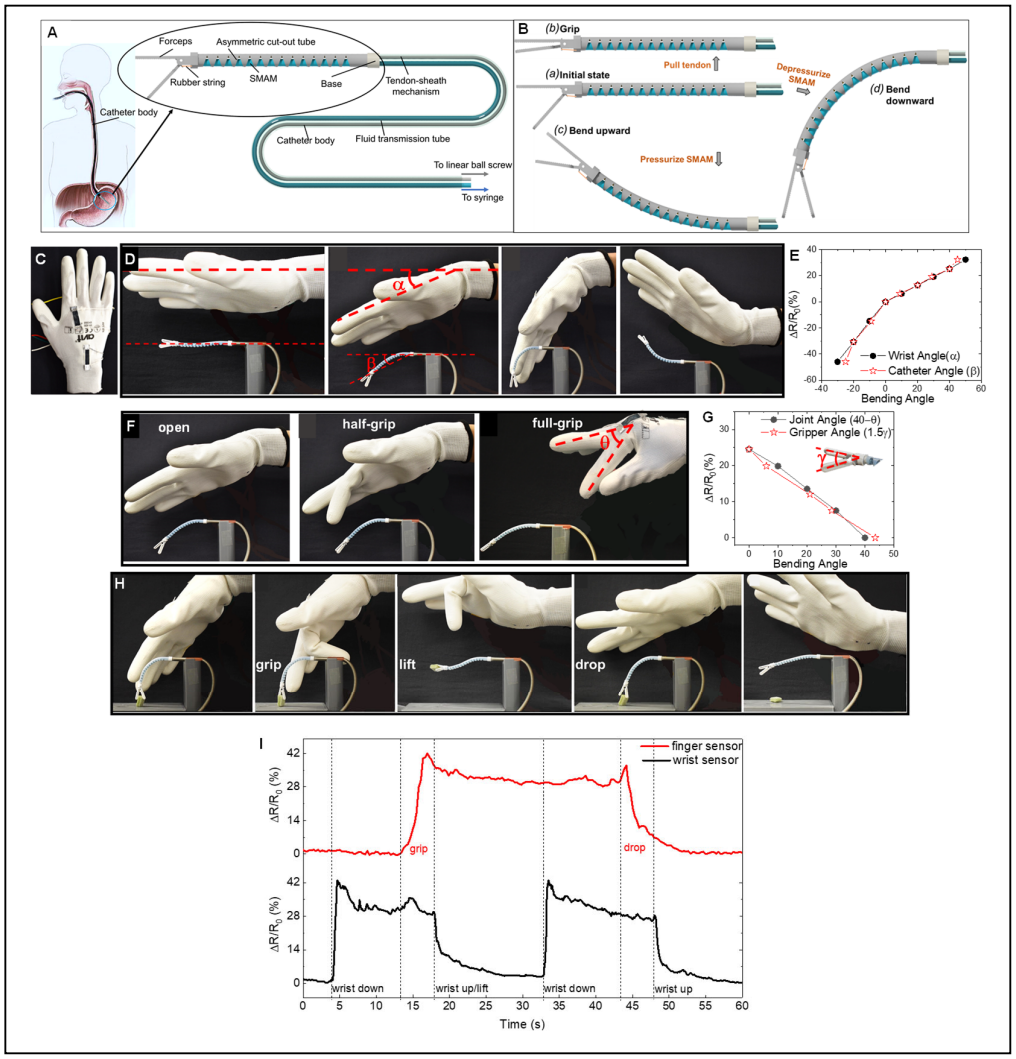

Figure 6. Demonstration experiment with the soft surgical tentacle gripper (**A**) The components and the potential use in the gastrointestinal tract. (**B**) The robotic catheter working principle. (a) Initial state, (b) gripping state, (c) bending upward state, and (d) bending downward state. (**C**) Two VT sensors were attached to a soft glove, which would be worn by the surgeon. (**D**) different range of catheter motion is shown. (**E**) The catheter bending angle (β) matches the wrist angle (α) by a factor of 99%. (**F**) The gripper could follow the hand gestures, demonstrating a half grip and a full grip. (**G**) The gripper angle (γ) matches the joint angle (θ) by a factor of 95%. (**H**) Demonstration of the capability of the tentacle gripper in bending, gripping, lifting, and then dropping an object. (**I**) The VT sensors' real-time responses to the motions shown in (**H**).

Unidirectional, Highly Linear Strain Sensors with Thickness-Engineered Conductive Films for Precision Control of Soft Machines

Saeb Mousavi, Mai Thanh Thai, Morteza Amjadi, David Howard, Shuhua Peng, Thanh Nho Do, Chun H. Wang

Supporting Information

Contents:

Effect of pre-stretching

An important factor that contributed to enhancing the sensors' performance is the pre-stretch level. Pre-stretching is a technique used in crack-based strain sensors for improving sensitivity and linearity [33]. The sensors exhibited enhanced sensitivity and linear strain range after pre-stretching at a higher strain. The results in Figures S1(C-E) show that when PEDOT, PEDOT-CNF and High-conc. PEDOT-CNF sensors were pre-stretched to 50%, 100% and 150% strain, respectively, their gauge factors were increased by 228% (from 127 to 417), 89% (from 147 to 278) and 71% (from 87 to 149), respectively. A comparison of the hysteresis behavior for as-made and pre-stretched sensors is presented in Figures S1C and D, indicating that without pre-stretching, the sensors have a wider hysteresis loop than after being pre-stretched. In addition, the pre-stretched sensor showed a much more stable response during the first 10 cycles with a significantly better linear working range.

Infill analysis

The actual printing density is calculated using the equation given in [31] and it is different from the nominal infill% set in the printer software (Simplify3D). The actual infill% values were calculated from the optical images shown in Figure S5. For infill densities greater than 90%, the printed tracks tend to randomly connect at different locations. In this case, we calculated the average infill density by measuring the infill density for all pairs of printed tracks in the image.

infill% $= \frac{b}{a}$ ("b" and "a" are shown in Figure S5(D))

80% nominal è $\frac{b}{a}$ = 56.6%

90% nominal è $\frac{avg(b)}{avg\ (a)}$ = 72.8%

100% nominal è $\frac{avg(b)}{avg\ (a)}$ = 97.2%

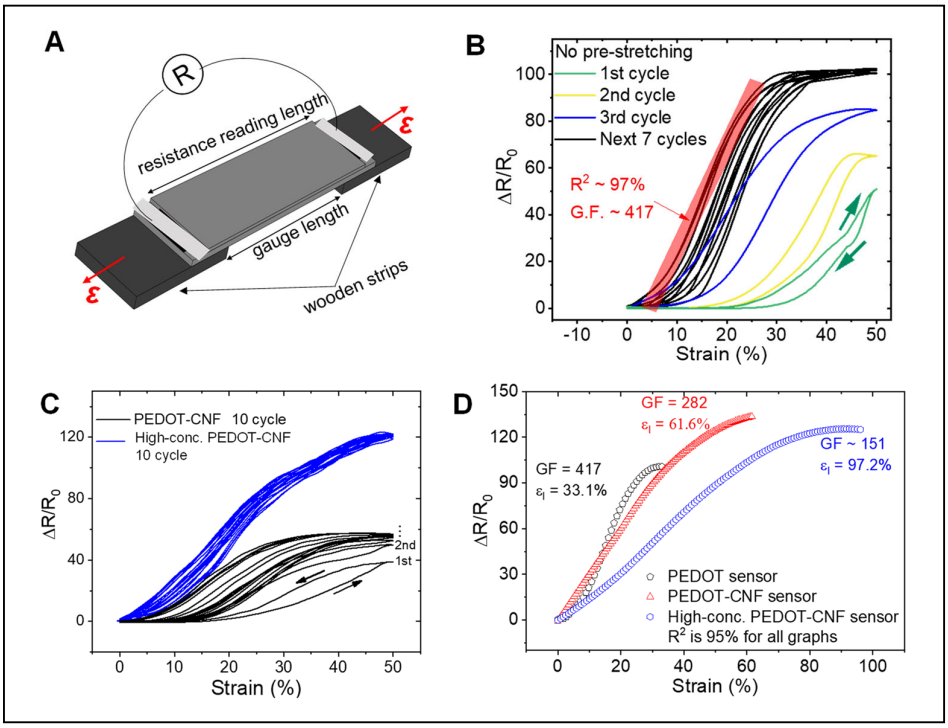

Figure S1. (**A**) The sensors were glued at the back on two wooden strips for tensile tests and the resistance is measured from outside the glued spots. (**B**) The resistance changes of the 3D printed PEDOT sensor in the strain domain for the first ten cycles of repeated stretching at 50% strain showing the effect of pre-stretching. (**C**) The resistance changes of the 3D printed PEDOT:PSS-CNF sensor for the first ten cycles of repeated stretching at 50% strain (black curves), and the resistance changes of the 3D printed PEDOT:PSS-CNF sensor for the ten cycles of repeated 50% stretching after being pre-stretched to 100% strain (blue). (**D**) The linear operation range of PEDOT sensor (ε_l ~ 33%), PEDOT:PSS-CNF sensor (ε_l ~ 61%), and high-conc. PEDOT:PSS-CNF sensors (ε_l ~ 97%) are shown in black, red, and blue, respectively.

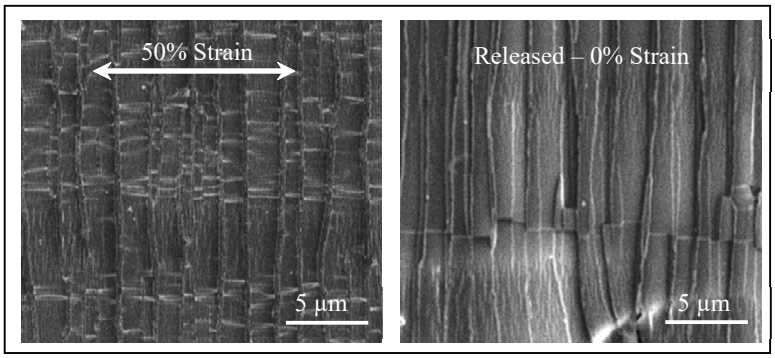

Figure S2. The Region *ii* of the PEDOT sensor under 50% strain and after strain release. Once the strain was released, the generated crack edges were re-connected.

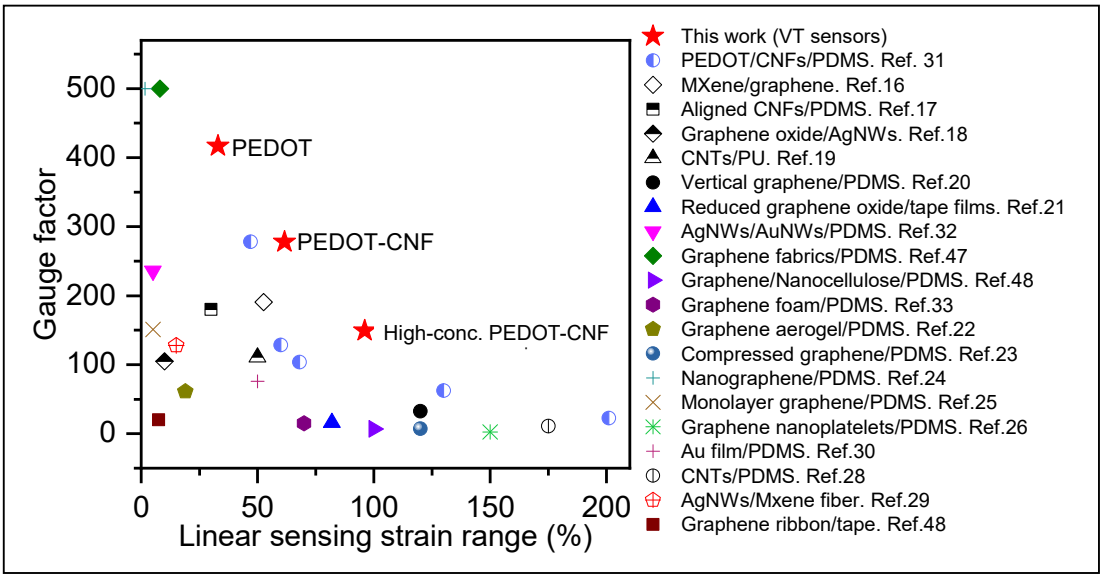

Figure S3. Comparison of sensing performance in terms of GF and linear sensing range of strain sensors in this work (PEDOT, PEDOT-CNF, and high-conc. PEDOT-CNF sensors) with the recently reported ones in the literature. The current sensors show superior performance compared to the previously reported sensors.

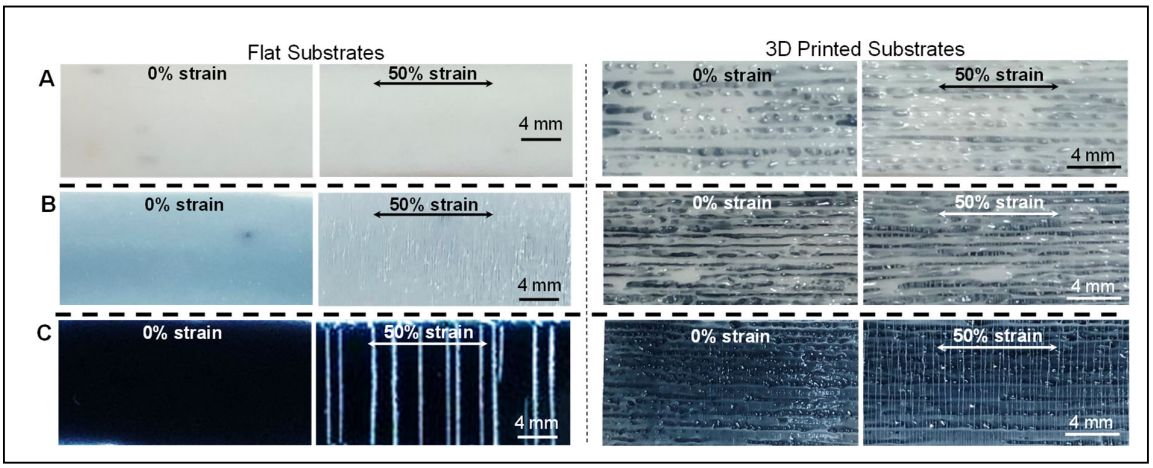

Figure S4. Crack morphology comparison between PEDOT sensors coated on flat and 3D printed substrates. (**A-C**) Optical images of the PEDOT sensors with a thickness of 42, 324, and 655 nm, respectively at rest (0% strain) and under 50% strain.

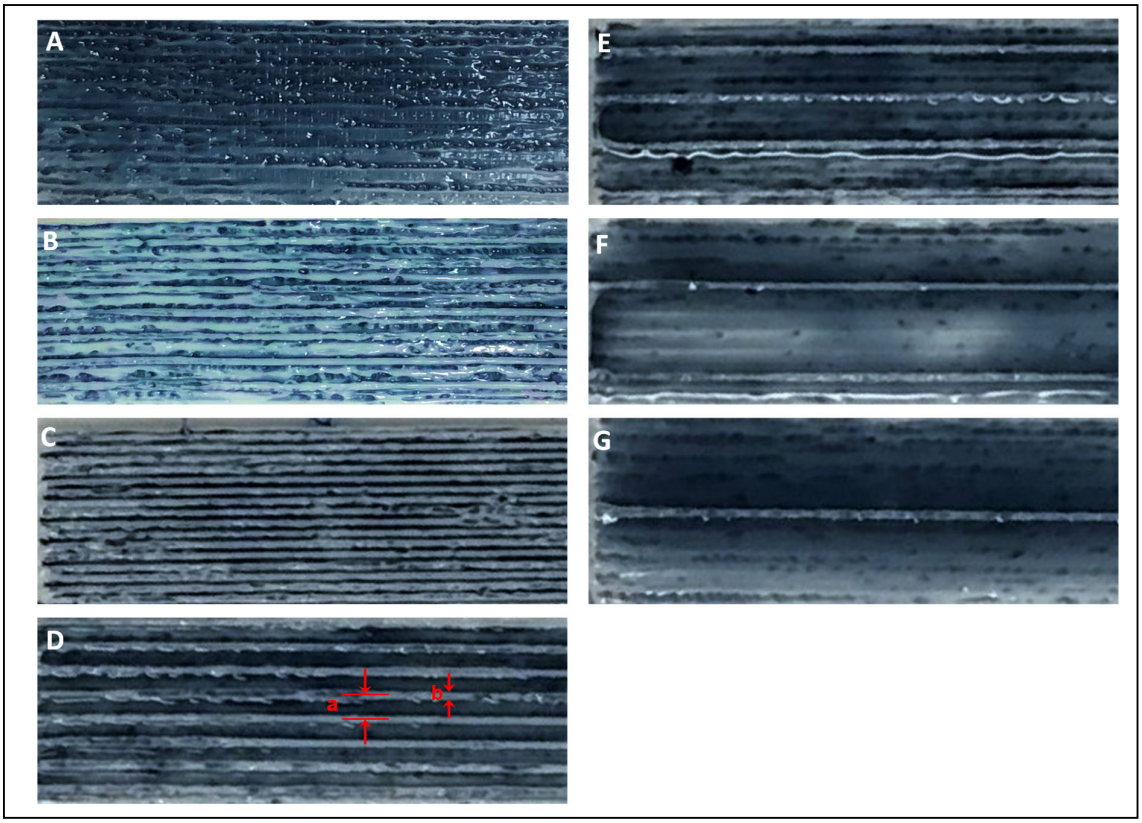

Figure S5. Top-view optical images of the PEDOT sensors coated on 3D printed TPU substrates with different infill densities: (**A**) 100%, (**B**) 90%, (**C**) 80%, (**D**) 40%, (**E**) 20%, (**F**) 10%, (**G**) 5%.

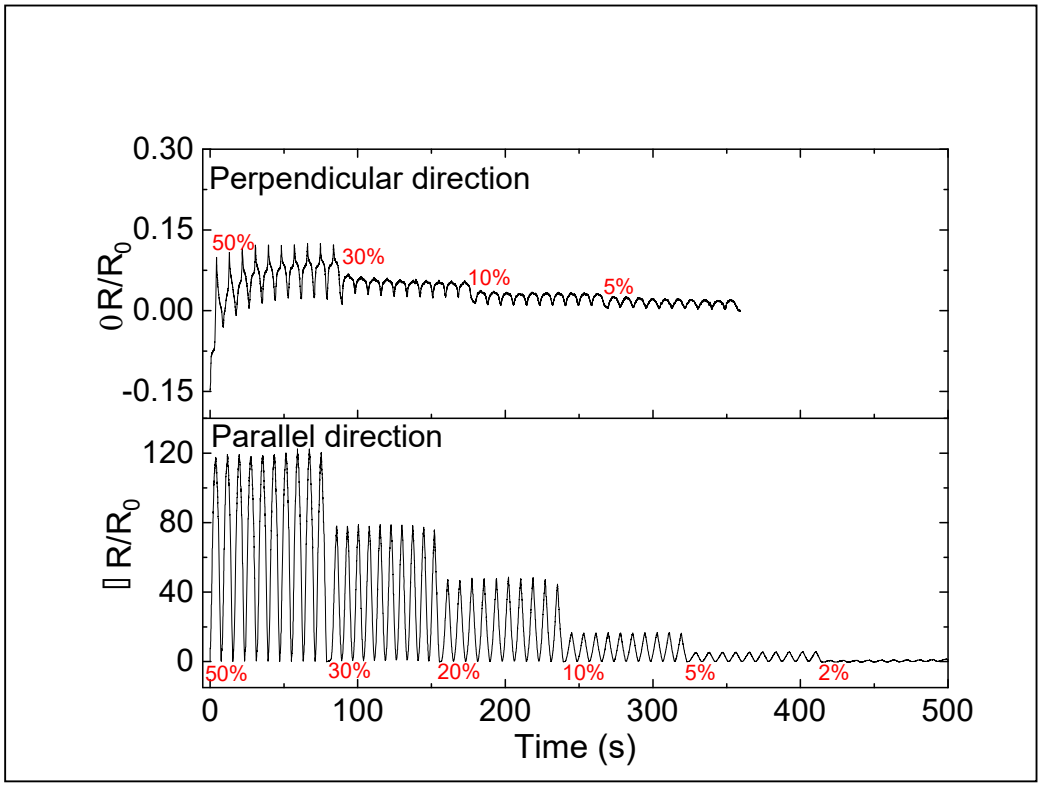

Figure S6. The resistance change of the VT sensor when stretched in parallel and perpendicular to the printing directions.

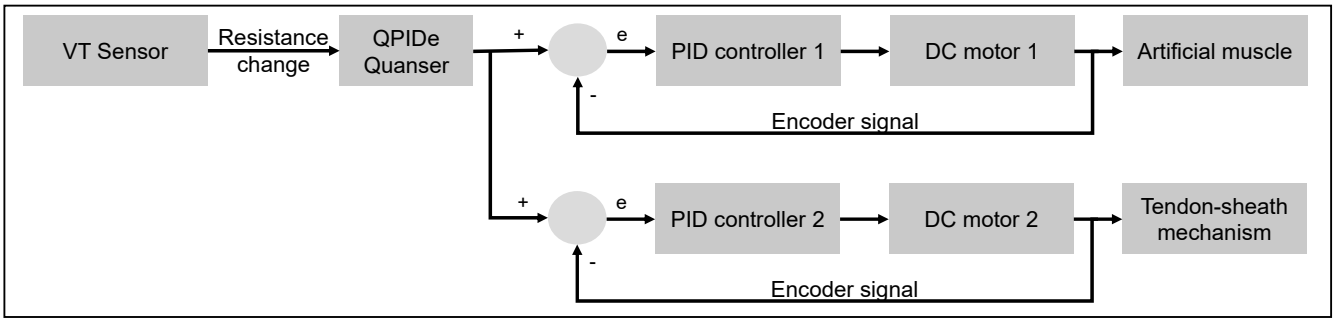

Figure S7. The control flow of the robotic catheter. The actuation commands in two DC motors are regulated by two simple PID controllers for the movement of each element of the robotic catheter, the gripper (tendon-sheath mechanism), and the tentacle (artificial muscle).

Movie S1. Demonstration of catheter control with our VT sensors

Table S1. 3D printing parameters for printing the TPU structure

Parameter	**Structural Material** TPU Ninjaflex (clear)
Filament Diameter (mm)	1.75
Nozzle Diameter (mm)	0.4
Nozzle Temperature (°C)	230
Bed Temperature(°C)	40
Printing Speed (mm/s)	500
Nominal Infill Density (%)	Variable for sensor substrate layer 100% for all other layers
Bottom Solid Layers (#)	1
Top Solid Layers (#)	0
Layer Height (mm)	0.2
Number of Shells	1
Track Width (mm)	450
Cooling Fan (%)	0
Support	None
Infill Pattern	Rectilinear
Raster Angle (°) (Print Direction)	0, 90 (alternating)